Laser and Particle Beams (1997), *vol.* 15, *no.* 4, *pp.* 607–626
Printed in the United States of America

The evolution of high-energy-density physics: From nuclear testing to the superlasers

By E. MICHAEL CAMPBELL, NEIL C. HOLMES, STEVEN B. LIBBY, BRUCE A. REMINGTON, AND EDWARD TELLER
Lawrence Livermore National Laboratory, Livermore, CA 94550, USA

(Received 24 October 1996; Accepted 10 July 1997)

We describe the role for the next-generation "superlasers" in the study of matter under extremely high-energy-density conditions in comparison with previous uses of nuclear explosives for this purpose. As examples, we focus on three important areas of physics that have unresolved issues that must be addressed by experiment: equations of state, hydrodynamic instabilities, and the transport of radiation. We describe some of the advantages the large lasers will have in a comprehensive, laboratory-based experimental program.

1. Introduction

The second half of the 20th century will be recorded as the dawning of the atomic era (McKay 1984; Teller 1987; Bethe 1995). As we prepare to close the century and the millenium, we mark yet another historic moment. With the signing of the Comprehensive Test Ban Treaty (CTBT), we have brought to a close the era of nuclear testing (Cerniello 1996; Goodwin 1996; Keeny & Cerniello 1996). A consequence of the treaty is that scientists will lose access to a regime of high-energy-density physics that has been difficult to attain by other known means. However, with the construction of the next generation of "superlasers" such as the National Ignition Facility (NIF) (Paisner *et al.* 1994) in the United States and the Laser MegaJoule project (LMJ) (Andre 1995; CHOCS No. 13 1995) in France, the capability to focus 1–2 MJ of energy into millimeter-scale volumes at power levels of 500 *TW* will become routine. These lasers are being built to spearhead the international effort in controlled nuclear fusion through inertial confinement fusion (ICF) (Nuckolls *et al.* 1972; Bodner 1974; Brueckner *et al.* 1974; Henderson *et al.* 1974; Lindl & Mead 1975; Lindl 1995) and to open new regimes for high-energy-density physics research (Hora 1991; Weisman 1995; Rosen 1996; Lee *et al.* 1995; Lawler 1997). With the advent of megajoule class lasers, the ability to access very high-energy-density regimes hitherto existing only at the cores of stars and in nuclear detonations will be partly recovered. The purpose of this paper is to give an overview of some of the regimes that the superlasers will be able to access that previously resided exclusively within the domain of nuclear detonation experiments. A preliminary, much briefer version of this report has appeared elsewhere (Campbell *et al.* 1995). The present results are taken largely from work done on the Nova laser at Lawrence Livermore National Laboratory (Campbell 1991). We will focus on three areas of application as illustrative examples: equations of state (Section 2), hydrodynamic instabilities (Section 3), and radiation physics (Section 4). These topics are representative of areas that have already been studied on Nova class lasers (Rosen 1996; Lee *et al.* 1995). However, a wide range of other possible topics, such as plasma physics with 10^7–10^8 Gauss local magnetic fields (Wilks *et al.* 1992; Bulanov *et al.* 1996; Pukhov 1996), potential experiments with the intense (10^{18}) neutron burst expected from the NIF capsule ignition, or

© 1997 Cambridge University Press 0263-0346/97 $11.00 + .10

https://doi.org/10.1017/S0263034600011186 Published online by Cambridge University Press

the physics of laser–matter interactions with the ultrahigh intensity, short pulse lasers (Wilks 1992; Tabak *et al.* 1993; Wilks *et al.* 1993; Perry & Mourou 1994; Hartemann *et al.* 1995; Bulanov *et al.* 1996; Mason 1996; Umstadter *et al.* 1995, 1996) ($I > 10^{20}$ W/cm^2) will not be addressed here. We summarize and conclude in Section 5.

2. Equation of state

One of the main goals of high-energy-density physics is to understand the behavior of matter at high pressure and density, that is, the equation of state (EOS) (Al'tshuler 1965; Eliezer *et al.* 1986; Eliezer & Ricchi 1991; Fortov & Kostin 1991; Avrorin *et al.* 1993). Areas of physics where EOS is relevant include basic condensed matter physics, planetary physics, geophysics, astrophysics, and ICF. Our understanding of other high-energy-density research, such as radiation transport and hydrodynamics, rely heavily on our knowledge of the state of the materials under study.

Shock compression is a widely used method for experimentally determining equations of state at high pressure. The Rankine-Hugoniot relations for shock compression of materials result from conservation of momentum, mass, and energy and are given by

$$P - P_0 = \rho_0 u_s u_p, \tag{1a}$$

$$\rho_0/\rho = 1 - u_p/u_s, \tag{1b}$$

$$E - E_0 = (P + P_0)(V_0 - V)/2, \tag{1c}$$

where P, $\rho = 1/V$, and E are the final pressure, density, and total energy, respectively, and P_0, $\rho_0 = 1/V_0$, and E_0 are their initial values. The shock and particle velocities are u_s and u_p, respectively. These relations allow the final shocked state to be determined by measuring the shock and particle velocities in the system. Figure 1a shows some data for the principal Hugoniot of Al (Young *et al.* 1985). The principal Hugoniot is the pressure-density curve for singly shocked material, starting from a cold, normal density solid. For pressures less than a few megabars, the data were taken using high explosives (HE) or gas guns to accelerate flier plates and have characteristic uncertainties below 1%. The data shown for pressures above a few megabars were taken during underground nuclear detonations. A single comprehensive EOS theory spanning density-temperature space is not yet in hand. Hence, when a global EOS is needed, a table is constructed by connecting the various model EOS results by interpolation (Young *et al.* 1985), as illustrated by the solid curve in figure 1a.

A number of different theoretical models for the EOS of Al are illustrated in figure 1b (Avrorin *et al.* 1987). The results are plotted for high pressure and compression ($P > 10$ Mbar, $\rho/\rho_0 > 3$), where the various models exhibit differences. The simplest and most widely used of the models is the statistical Thomas-Fermi model with quantum corrections (TFQC) (Kopyshev 1977; Trunin 1994), shown by the solid curve, which corresponds to the high temperature, $T > 10$ eV, region of the tabular EOS shown in figure 1a. This model does not include atomic shell structure but rather treats the electron states as a continuum. The self-consistent field (SCF) (Sin'ko 1979; Trunin 1994), Hartree-Fock-Slater (HFS) (Nikiforov 1978, 1979, 1989; Trunin 1994), and INFERNO (Liberman 1982) models treat the electron shells quantum mechanically but differ in their handling of close-packed levels corresponding to energy bands. The semiclassical equation of state (SCES) model (Nikiforov 1978, 1979, 1989; Andriyash & Simoneko 1984) treats both the discrete electron shells and the energy bands semiclassically. The ACTEX model (Rogers 1981) is an ionization equilibrium plasma model that uses effective electron–ion potentials fitted to experimental spectroscopic data. These models typically include the nuclear component using the ideal gas approximation. An exception is a Monte Carlo treatment of the thermal motion of the nuclei implemented in one of the versions of the SCES (Kopyshev 1977; Nikiforov 1978, 1979, 1989). For low-Z materials, the statistical treat-

https://doi.org/10.1017/S0263034600011186 Published online by Cambridge University Press

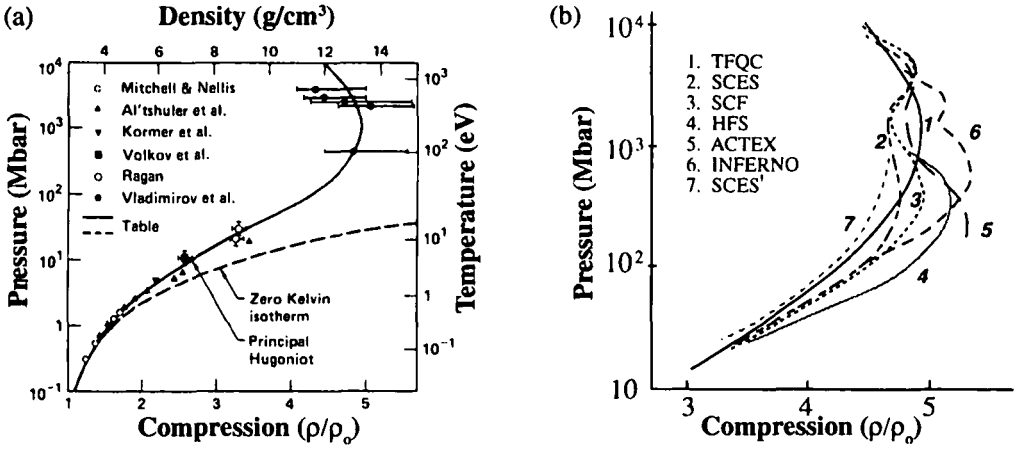

FIGURE 1. (a) A comparison (reproduced from Young *et al.* 1985) of experimental and tabular theoretical shock Hugoniots for Al. Temperatures calculated from the table are indicated on the right vertical axis, and the 0 K isotherm is also shown for comparison. (b) Calculations of the principal Hugoniot of aluminum using a variety of theoretical methods (from Avrorin *et al.* 1987).

ment of the electrons in the Thomas-Fermi approach fails because of the strong atomic shell effects (see figure 1b); there are no adequate theories for low-Z fluid metals.

The oscillations in the theoretical pressure versus compression curves shown in figure 1b result from the pressure ionization of the K- and L-shell electrons of Al. At pressures of 100–500 Mbar, ionization of the L-shell electrons occurs as a result of the high compression, which forces neighboring atoms sufficiently close together to disrupt the $n = 2$ electron orbital. Pressure ionization is an efficient energy sink whereby compression causes electrons to be liberated but at little appreciable increase in pressure. Hence, at the onset of pressure ionization, the material becomes more compressible, exhibiting a "softer" EOS. Once ionization from the shell is complete, the effect is a "hardening" of the EOS because there are now many more particles (electrons + ions) contributing to the pressure. A similar softening–hardening oscillation is predicted to occur at pressures of 3–5 Gbar due to ionization of the K-shell electrons, although the magnitude of the effect is smaller due to the lower number of K electrons. This pressure–ionization effect on the EOS is qualitatively similar to that due to molecular dissociation of N_2 and D_2, which has been experimentally observed at lower pressures (Nellis *et al.* 1984, 1991; Radousky *et al.* 1986; Ross 1987; Holmes *et al.* 1995).

There exists considerable theoretical uncertainty in the EOS of Al in the pressure range of 50–1000 Mbar, where the electron quantum shell effects become important and absolute data are missing, sparse, or have large uncertainty. Large lasers have the potential to fill in the experimental curves for many materials in this critical range of 10–1000 Mbar. Recall that the principal Hugoniot of materials is determined absolutely by simultaneous measurements of particle and shock velocities [see equation (1)]. The shock velocity is typically measured by recording the shock breakout times across known step heights of the sample under investigation. Determining the particle velocity is generally more difficult. It has been measured successfully in nuclear-driven experiments using gamma-reference layers (Simonenko *et al.* 1985) and neutron resonance Doppler shifts (Ragan *et al.* 1977). The gamma technique uses thin planar layers implanted into the material under study; europium has been used, which has a large (n,γ) neutron-capture cross section. During nuclear detonation, large neutron fluxes are produced, which, after being moderated to thermal energies, turn the reference layer into a strong gamma source. Because the reference layers flow with the bulk flow, the γ-ray emission can be viewed through collimated viewing slits from the side to deduce the mass velocity. The

https://doi.org/10.1017/S0263034600011186 Published online by Cambridge University Press

neutron resonance technique differs in that the mass velocity is determined by measuring the Doppler shifts of low-energy neutron resonances in the material behind the shock.

Two approaches are being pursued on lasers for determining the principal Hugoniot of materials. An absolute method employs X-ray side-lighting to simultaneously measure u_s and u_p in a shock-compressed sample (Hammel *et al.* 1993, 1994; Cauble *et al.* 1997). An example from a recent experiment (Cauble *et al.* 1997) using the Nova laser is shown in figure 2a. The target was a composite consisting of a 200-μm-thick layer of CH(Br), that is, plastic doped with bromine ($C_{50}H_{48}Br_2$), at a density of $\rho = 1.2$ g/cm^3, which served as the "piston." This piston is backed by a 2-mm-thick layer of CH at a density of 1.0 g/cm^3, which is the material under investigation. Nova (Campbell 1991) is a Nd:glass laser with 10 arms, each capable of generating over 3 kJ of energy at the third harmonic, $\lambda_{Laser} = 0.351$ μm, in ~nanosecond pulses. It is typically run in "indirect-drive" mode, where the laser light converts to X rays in a millimeter-scale gold cylindrical cavity or hohlraum. The target for this EOS experiment is driven on the CH(Br) side by a ~200-eV thermal X-ray drive that is generated by focusing 28 kJ of laser light from eight arms of the Nova laser in 2 ns into the hohlraum. The rapid, intense flux of X-rays incident on the open face of the planar CH(Br) target launches a strong shock, several tens of megabars, through the target. After being shocked, the CH(Br) behaves like an opaque piston, shock compressing the CH. This composite target is illuminated from the side with a source of 5-keV hard X rays, whose transmission is imaged in one dimension with a pinhole X-ray imager and time resolved (streaked) in the other dimension. Prior to compression, the optical depths of the CH and CH(Br) viewed from the side were 0.8, and 5, respectively. After compression, these values increased to 3 and 20. Hence, the pre- and postshocked CH are clearly observed in transmission, but the CH(Br) "piston" is essentially opaque at all times. The piston–CH boundary, however, is clearly resolved at all times and determines the particle velocity. After calibrating the temporal sweep rate of the X-ray streak camera and the

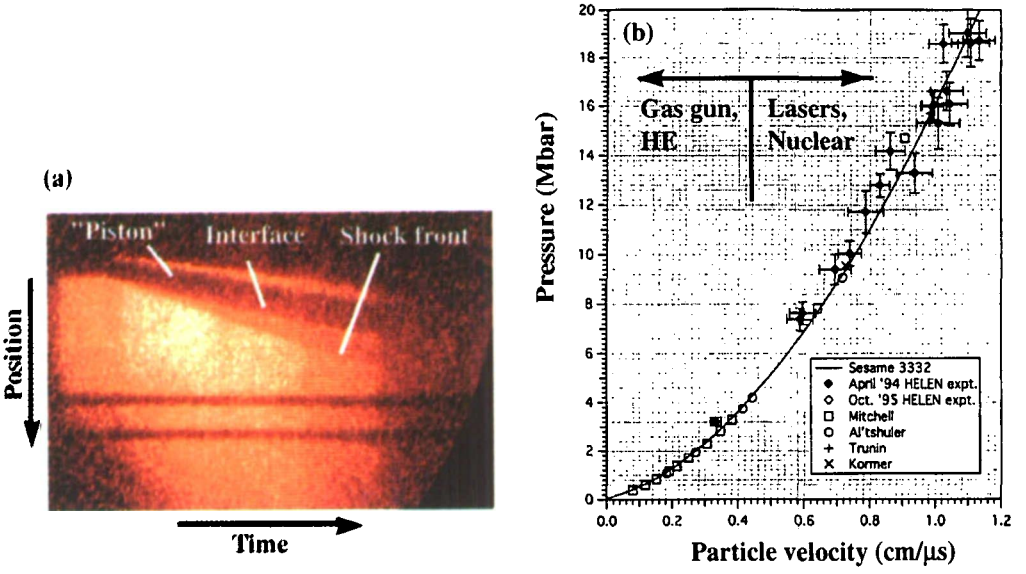

FIGURE 2. (a) Initial results from an experiment of Cauble *et al.* (1997) using the Nova laser to measure the EOS of CH. The time-resolved 1D image shows the interface between the CH(Br) "piston" and the CH being compressed, and the shock front moving ahead into the CH. (b) Relative EOS measurements for Cu from Rothman *et al.* (1996) using the Helen laser at AWE and the impedance matching technique. Superposed are results from the Sesame EOS tables and from other experiments from both using gas guns and from nuclear detonations.

https://doi.org/10.1017/S0263034600011186 Published online by Cambridge University Press

overall magnification of the imaging system, the two velocities, shock velocity (u_s) and particle velocity (u_p), can be determined. Equation (1) then gives the principal Hugoniot, namely, $P(u_p)$. A preliminary analysis of figure 2a produces a compression of about 3 for an applied "piston" pressure of about 20 Mbar. A similar experiment has recently been conducted on cryogenic deuterium, D_2, to measure its principal Hugoniot at ~1–2 Mbar, the region where molecular dissociation softens its EOS (DaSilva *et al.* 1997). Improvements in the experimental precision currently under development should turn this type of absolute measurement into a powerful technique for high-pressure EOS research.

The second technique used in laser EOS measurements is the impedance matching method (Zel'dovich & Raizer 1967; Mitchell *et al.* 1991; Fu *et al.* 1995; Koening *et al.* 1995; Evans *et al.* 1994, 1996a,b; S.D. Rothman, personal communication 1996). This technique relies on comparing shock velocities in a reference material of known EOS, oftentimes Al, with that in a test sample. The target typically consists of a baseplate of Al, upon which the test samples are mounted, one of which is also an Al step. By measuring the shock breakout times from the Al baseplate, the Al step, and the test sample step, the shock velocities u_s in both the reference Al and in the test sample can be determined. Applying equation (1) and the fact that P and u_p are continuous across the interface between the Al baseplate and test sample allows one point on the $P(u_p)$ curve to be determined. Results from a series of such measurements by Rothman and others (Evans *et al.* 1994, 1996a,b; S.D. Rothman, personal communication 1996) using the AWE Helen laser led to the experimental EOS of Cu up to a pressure of 20 Mbar (figure 2b). These experimental results are compared with the Sesame EOS table (Holian 1984) and with previous experimental determinations from gas guns and nuclear explosions. All the data for Cu above 5 Mbar were obtained either on a nuclear detonation (Mitchell *et al.* 1991) or on a laser experiment (Evans *et al.* 1994, 1996a,b; S.D. Rothman, personal communication 1996). The gas gun data is limited to pressures lower than approximately 5 Mbar. This type of laser EOS experiment could be extended to nearly gigabar pressures on existing laser facilities with the use of flier plates (Faral *et al.* 1990; Cauble *et al.* 1993). Higher pressures yet are anticipated for the next generation of superlasers.

Even though the precision of the laser EOS experiments still needs improving, it is clear from figure 2b that lasers currently offer the best and perhaps only avenue to experimental EOS investigations at $P > 10$ Mbar, which is where most of the uncertainties in the theories reside. One unique feature of lasers is the ability to easily temporally shape the laser power profile. This feature allows experiments that use a series of staged shocks to compress a sample nearly adiabatically (Nuckolls *et al.* 1972; Lindl 1995). Such a capability is of interest from an astrophysical point of view because one could achieve states of matter similar to the cores of giant planets and brown dwarfs (Stevenson 1975, 1976; Hubbard & De Witt 1985; Marley & Hubbard 1988; Saumon & Chabrier 1992; Hubbard *et al.* 1995; Hubbard 1997). There are uncertainties in our understanding of the cores of the giant planets due to the possibility of a plasma phase transition (insulator to metallic) in the hydrogen (Nellis *et al.* 1995; Weir *et al.* 1996), which would affect the density of the core. There is an even greater uncertainty arising from the possibility of a miscibility phase transition. At sufficiently high densities but low temperatures, He and the "metals" ($Z > 2$) may become immiscible with metallic hydrogen by separating out and sinking to the core (Stevenson 1975, 1976; Hubbard & De Witt 1985; Marley & Hubbard 1988; Saumon & Chabrier 1992; Hubbard *et al.* 1995; Hubbard 1997). This would provide a source of gravitational energy and would change the opacity of the outer atmosphere. With careful pulse shaping using the future superlasers, one may be able to approach the relevant high-density but cool 1–50 Mbar states of matter (Meyer-ter-Vehn & Oparin 1995).

There remain a number of challenges for laser experiments to overcome. The first is the generation of constant-velocity planar shocks (Löwer & Sigel 1993; Löwer *et al.* 1994). Second, the elimination of preheat of the samples by electrons or radiation from the hohlraum and

https://doi.org/10.1017/S0263034600011186 Published online by Cambridge University Press

from the ablation region is required (Löwer & Sigel 1993; Löwer *et al.* 1994). Third, at extremely high pressures, the material behind the shock front will be highly ionized and will become a strong source of X rays. Radiative preheat of the material ahead of the shock front could become a significant effect (Zel'dovich & Raizer 1967; Young *et al.* 1985), and experiments to test current understanding should become possible on the superlasers.

The small spatial scales and fast time scales of laser experiments also offer unique advantages for the study of solid-state material structure at high pressures and extremely high strain rates. The size and geometry of both nuclear and standard gas gun impact methods make X-ray measurements extremely difficult. However, such measurements are straightforward with lasers and have been developed by Wark and others to determine lattice structure under laser-induced shock compression (Wark *et al.* 1987, 1989; Zaretskii *et al.* 1991). We illustrate the technique in figure 3 with results from a recent solid-state compression experiment by Kalantar *et al.* (1997a; Hauer *et al.* 1996; Wark *et al.* 1990, 1992, 1996; Woolsey & Wark 1997) who used the Nova laser to generate the X-ray drive that launched the shock. In this experiment, the X-ray drive is incident on a 40-μm-thick piece of (111) orientation single-crystal Si, launching a few hundred kilobar shock through the sample. The Si foil is probed across the back side using Bragg diffraction from a 5.2-keV source of vanadium He-α X rays at a Bragg angle of 22° and is recorded with a streaked (time-resolved) crystal spectrometer. Early in time, only the Bragg peak for uncompressed Si, centered horizontally in the image, is apparent in figure 3a. About halfway through the sweep at ~4 ns (halfway up the image), both shocked and unshocked Si are being probed simultaneously, due to the ~20-μm mean free path of 5.2-keV X rays in Si. After the shock breaks out the back side of the Si, the crystal relaxes back to its original density, ρ_0, but starts to lose the integrity of its lattice structure at the back face, perhaps indicating the onset of spallation. The Bragg peak for the shock-compressed Si is reduced in height as opposed to the uncompressed peak. This DeBye-Waller effect is due to the thermal motion of the lattice from the shock-imparted heating (Kittle 1976; J. Wark, personal communication 1996) and in principle can be used to infer the temperature of the shocked sample. A profile just prior to shock breakout is given in figure 3b, which shows the clean separation between the unshocked and shocked Bragg peaks. The clean separation between the two peaks illustrates the sharp, planar nature of the shock launched with the X-ray drive, such

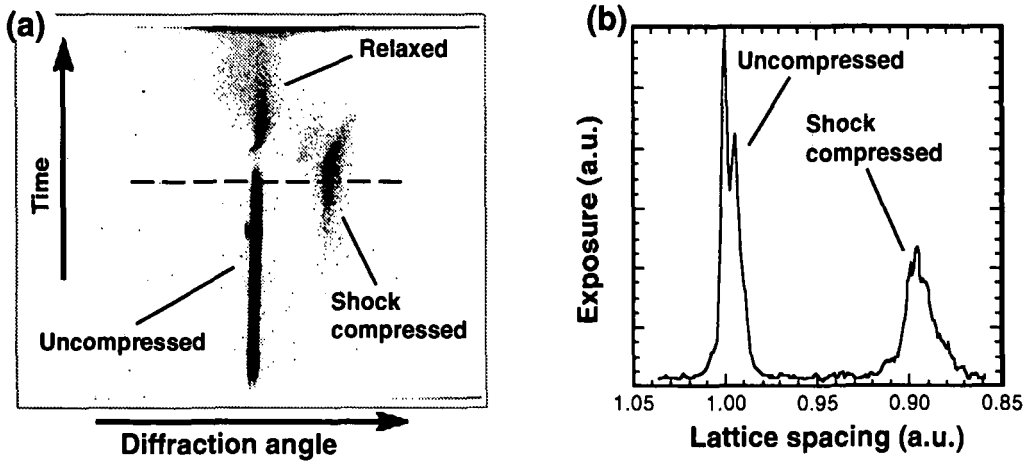

FIGURE 3. (a) Initial experimental results of Kalantar *et al.* (1997) and Woolsey and Wark (1997) using the Nova laser to shock a sample of single-crystal Si maintained in the solid state. The lattice under compression is diagnosed by time-resolved Bragg diffraction. The initial Bragg angle was 22° off the back-side of a 40-μm-initial-thickness Si sample, using a V He-α point backlighter at 5.2 keV. (b) Profile taken at the time indicated by the dashed horizontal line in (a) showing the Bragg peaks corresponding to the uncompressed and compressed Si as the shock nears the back surface.

https://doi.org/10.1017/S0263034600011186 Published online by Cambridge University Press

that the density of the Si probed is either ρ_0 (uncompressed) or ρ_1 (compressed) but nothing in between.

One of the key open areas of solid-state physics to be investigated with this type of experiment is the transition from 1D to 3D compression, and in particular the rate at which this transition takes place. The most recent work in this area by Whitlock and Wark (1995) demonstrated that the axial (1D) and lateral (3D) compression of a crystal could be measured simultaneously using Bragg diffraction off the back side, as described above, together with transmission Laue diffraction. They concluded that the crystal compresses initially in 1D but quickly relaxes to a 3D compressed state, exhibiting compression both axially and laterally. This 1D-to-3D relaxation due to the elastic–plastic transition is a phenomenon whose time duration is of fundamental interest to slid-state physics (Meyers 1994). This type of experimental research could have a profound influence on the theory of solids under shock compression.

3. Hydrodynamic instabilities

Hydrodynamic instabilities and the material mixing they cause occur ubiquitously throughout nature. The situation in a nuclear detonation is no exception. However, in this case, the instabilities arise under extreme conditions of temperature and density in the presence of a strong radiation field. This situation is not unique to nuclear detonations, but also occurs in supernova explosions (Müller *et al.* 1991), astrophysical radiative shocks (Luo & McCray 1991, 1994; Suzuki *et al.* 1993; Klein *et al.* 1994; Chevalier & Blondin 1995), and in ICF implosions (Bodner 1974; Brueckner *et al.* 1974; Henderson *et al.* 1974; Lindl & Mead 1975; Lindl 1995; Rosen 1996). The three most common hydrodynamic instabilities are the acceleration-driven Rayleigh-Taylor (RT) instability, its shock analog the Richtmyer-Meshkov (RM) instability, and the shear-induced Kelvin-Helmholtz (KH) instability. The typical situation for the RT instability occurs at an interface between a low-density (ρ_2) fluid and a high-density (ρ_1) fluid. If the lighter fluid is accelerating the heavier fluid, then in the frame of reference of the interface one effectively has a heavy fluid "sitting on top of" a light fluid. The interface is hydrodynamically unstable, and spatial perturbations η_0 will grow exponentially in time, $\eta(t) = \eta_0 e^{\gamma t}$. Classically, the growth rate in the linear regime is given by $\gamma = (Akg)^{1/2}$, with $A = (\rho_1 - \rho_2)/(\rho_1 + \rho_2)$ being the Atwood number, and $k = 2\pi/\lambda$ the perturbation wave number. In the nonlinear asymptotic limit, the interface evolves into bubbles of the lighter fluid rising at their terminal velocity of $v_B \approx 0.3\ (g\lambda)^{1/2}$ (for $A \approx 1$) and into spikes of the heavier fluid falling through the lighter fluid.

A convenient categorization of the flow is given by the dimensionless Reynolds number, $R = Lu/\nu$, where L is the system size, u the characteristic fluid velocity, and ν the kinematic viscosity. Situations of high R ($>10^3$) are prone to turbulent hydrodynamic mixing. Large spatial size L means that a large number of modes *could* grow; low-viscosity ν means that a broad range of modes *do* grow; and high-fluid-velocity u hastens the transition to turbulence through strong KH-driven vorticity generation. The situation in a plasma is similar except for compression and ionization. Compression introduces an additional scale to the problem, namely the density-gradient scale length, which affects dominant mode selection. Ionization causes the viscosity to drop to very low values, thereby causing plasmas to be extremely unstable hydrodynamically. Despite their small spatial scales, laser-produced plasmas can have Reynolds numbers in excess of 10^6 at high compression.

One long-used method of investigating shock-induced mixing due to the RM instability is the use of shock tubes (Brouillette & Sturtevant 1994; Vetter & Sturtevant 1995; Bonazza & Sturtevant 1996). With this method, the acceleration is impulsive, the pressures are typically only a few bars, the compression is low, and there is no radiation or ionization involved. High explosives generate pressures of up to 200–300 kbar (Benjamin & Fritz 1987), but compression is low, there is minimal or no ionization or radiation, and diagnostic access is limited. Gas guns can generate pressures up to a few megabars and large perturbation growth but with

https://doi.org/10.1017/S0263034600011186 Published online by Cambridge University Press

modest compression, diagnosis is difficult, and there is little radiation or ionization (Holmes *et al.* 1984; Holmes 1991). Macroscopic fluid–cell accelerators (Read 1984; Youngs 1984; Jacobs & Catton 1988; Kucherenko *et al.* 1991, 1993; Dimonte *et al.* 1996b; Jacobs & Sheeley 1996; Schneider *et al.* 1997) deal with incompressible hydrodynamics at modest accelerations (1–1000 g_0). Perturbation growth factors can be large, diagnosis can be good, but there is no radiation, ionization, or compression involved. On large lasers such as Nova and the NIF, the accelerations are extreme (10^{13}–10^{14} g_0), and pressures of hundreds of megabars are routine. We can achieve high growth factors, large compression, and high levels of radiation flow and ionization in arbitrary geometry (planar, cylindrical, spherical, or other). The situation in a nuclear detonation is similar, but all of the scales are larger.

One of the unique features of laser experiments is the degree of precision possible in selecting the initial conditions of experiments. An excellent example is the recent experimental verification by Marinak *et al.* (1995; Remington *et al.* 1996b, 1996c) of the differences between 2D and 3D RT-induced perturbation growth (figure 4). The experiment was conducted by preimposing a precisely formed perturbation on one side of a ~60-μm-thick plastic foil doped with bromine, $C_{50}H_{47}Br_3$, or CH(Br). This foil is then placed across an opening on a laser hohlraum wall, which, when pulsed with a ~200-eV radiation drive, is ablatively accelerated at ~75 $\mu m/ns^2$. The perturbations at the ablation front grow due to the RT instability. The three perturbations studied in Marinak *et al.* all had the same magnitude wave vector, $k = (k_x^2 + k_y^2)^{1/2}$ and the same amplitude, ~2.5 μm, differing only in their shape: 3D square $k_x = k_y$ ($\lambda_x = \lambda_y = 71$ μm), 3D stretched $k_x = 3k_y$ ($\lambda_x = 53$ μm, $\lambda_y = 158$ μm), and a 2D ripple $k = k_x = k_{2D}$ ($\lambda_{2D} = 50$ μm). The images shown in figure 4a–c correspond to time-resolved, face-on, in-flight radiographs taken of the accelerated planar foils. Dark regions correspond to spikes and bright regions to bubbles. The growth *versus* time of the fundamental mode Fourier amplitudes of the perturbations is shown in figure 4d. In the linear regime, all three modes grow at the same rate, as expected from linear theory, because they all have the same magnitude wave vector. But in the nonlinear regime, the square $k_x = k_y$ mode grows the largest, the 2D $k = k_x$ ripple grows the least, and the 3D stretched $k_x = 3k_y$ perturbation falls in between. This nonlinear shape effect has been predicted theoretically by several groups (Nishihara & Sakagama 1990; Tryggvason & Unverdi 1990; Town & Bell, 1991; Dahlburg *et al.* 1993; Hecht *et al.* 1994, 1995; Shvarts *et al.* 1995) but has not been observed experimentally until these laser experiments. As pointed out by Hecht *et al.* (1994, 1995; Shvarts *et al.* 1995), this shape effect can be understood qualitatively in terms of a simple buoyancy-*versus*-drag argument. In the asymptotic limit of terminal bubble velocity, the buoyancy is exactly balanced by the kinematic drag. At the bubble tip, the ratio of drag to buoyancy is smallest for the square mode, $k_x = k_y$, which consequently has the highest terminal bubble velocity and therefore grows the fastest.

Precise experiments of this nature also can be carried out in convergent geometries, as illustrated in figure 5, with preliminary results from two new experiments on the Nova laser. Glendinning *et al.* (1997) and Cherfils *et al.* (1997a,b) measured the growth of a 3D $k_x = k_y$ square-mode perturbation (here, $\lambda_x = \lambda_y = 100$ μm) but in spherically converging geometry. In the present paper, the perturbation was imposed on the outer surface of a ~500-μm-diameter hemisphere of CH(Ge), that is, $C_{50}H_{48.8}Ge_{1.2}$, which was mounted on the wall of a hohlraum, facing inward. Because the hemisphere is ablatively accelerated, the perturbations grow due to ablation from RT instability as the hemisphere converges. This result is illustrated in figure 5a with a sequence of face-on radiographs. Examination of $\lambda_{x,y}$ *versus* time (not shown) shows a decrease from 100 μm to 60 μm, indicating a total convergence, R_0/R, of just under 2. Analysis of the growth of the fundamental and second harmonics of the perturbation in terms of δ (optical depth) *versus* time shows that the perturbation enters the nonlinear regime at ~2 ns, as determined by the appearance of the second harmonic (not shown). The growth factor (GF) at this time is only 2.0–2.5. On a planar foil, this amount of growth for an $\eta_0 =$

https://doi.org/10.1017/S0263034600011186 Published online by Cambridge University Press

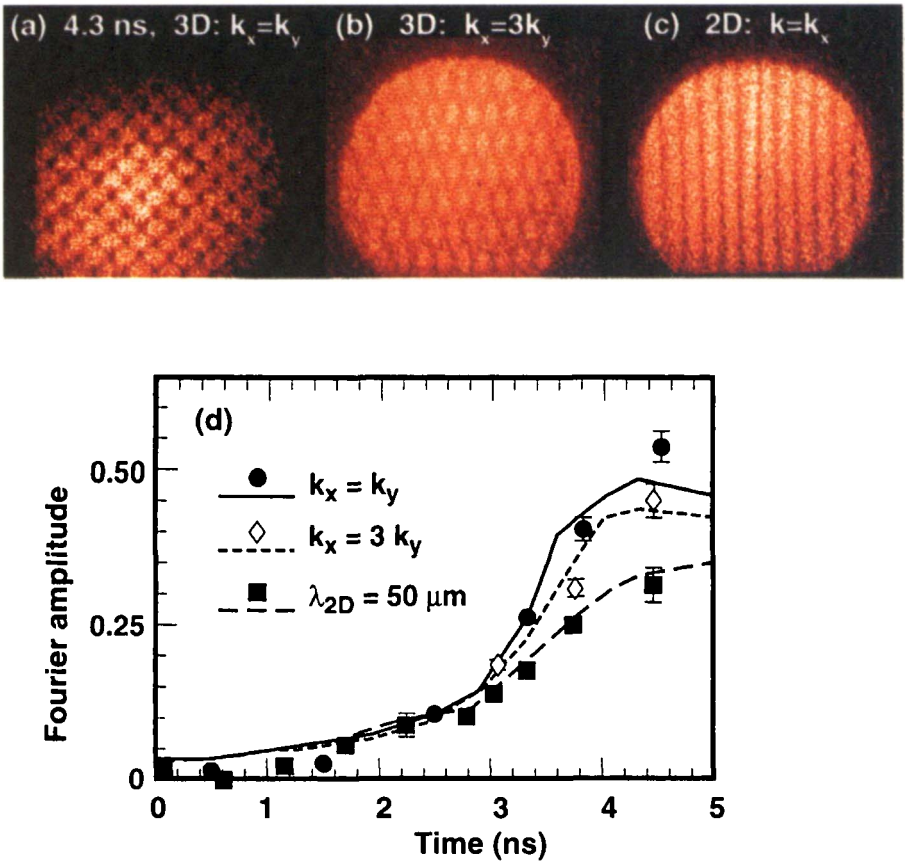

FIGURE 4. Experimental demonstration by Marinak *et al.* (1995) of the 3D shape effects of the Rayleigh-Taylor (RT) instability in the nonlinear regime. Images in (a)–(c) represent face-on, in-flight radiographs at 4.3 ns from three different experiments done on the Nova laser to measure RT-induced perturbation growth at the ablation front of accelerated planar foils of CH(Br), initially ~60 μm thick. The perturbations all had the same amplitude (~2.5 μm) and magnitude wave vector, $k = (k_x^2 + k_y^2)^{1/2}$. The perturbation shapes were (a) 3D square $k_x = k_y$ ($\lambda_x = \lambda_y = 71\ \mu$m), (b) 3D stretched $k_x = 3k_y$ ($\lambda_y = 53\ \mu$m, $\lambda_y = 158\ \mu$m), and (c) 2D, $\lambda_{2D} = 50\ \mu$m. (d) The growth in modulated optical depth of the fundamental mode Fourier amplitude *versus* time. All three shapes grow identically in the linear regime but differ in the nonlinear regime, with the square mode growing the most and the 2D ripple growing the least.

2.5 μm, $\lambda_x = \lambda_y = 100\ \mu$m perturbation would still be in the linear regime because $\eta/\lambda < 10\%$. The early entry into the nonlinear regime observed is due to convergence, that is, the wave length decreasing from 100 μm to 60 μm. For the same overall growth of η, η/λ is larger because λ is smaller, and the RT evolution has consequently entered the nonlinear regime. The flexibility of laser experiments allows such precise 3D nonlinear shape effects to be studied under nearly identical conditions in planar, spherical, cylindrical, or potentially arbitrary geometries.

Time-resolved radiography also has been done by Kalantar *et al.* (1997b) on implosions of perturbed Ge-doped CH capsules located at the center of hohlraums (figure 5b). The perturbation pattern imposed was a set of three grooved rings, even ~100 μm wide and ~3 μm deep, separated by 210 μm and 160 μm. The drive was the same as that used for the hemisphere experiments (figure 5a), and the convergence, $R/R_0 \approx 2$, was similar. The perturbation growth is clearly visible as dark bands corresponding to spikes and light bands to bubbles and compares very well with the simulation, as shown by the image at the far right in figure 5b. The

https://doi.org/10.1017/S0263034600011186 Published online by Cambridge University Press

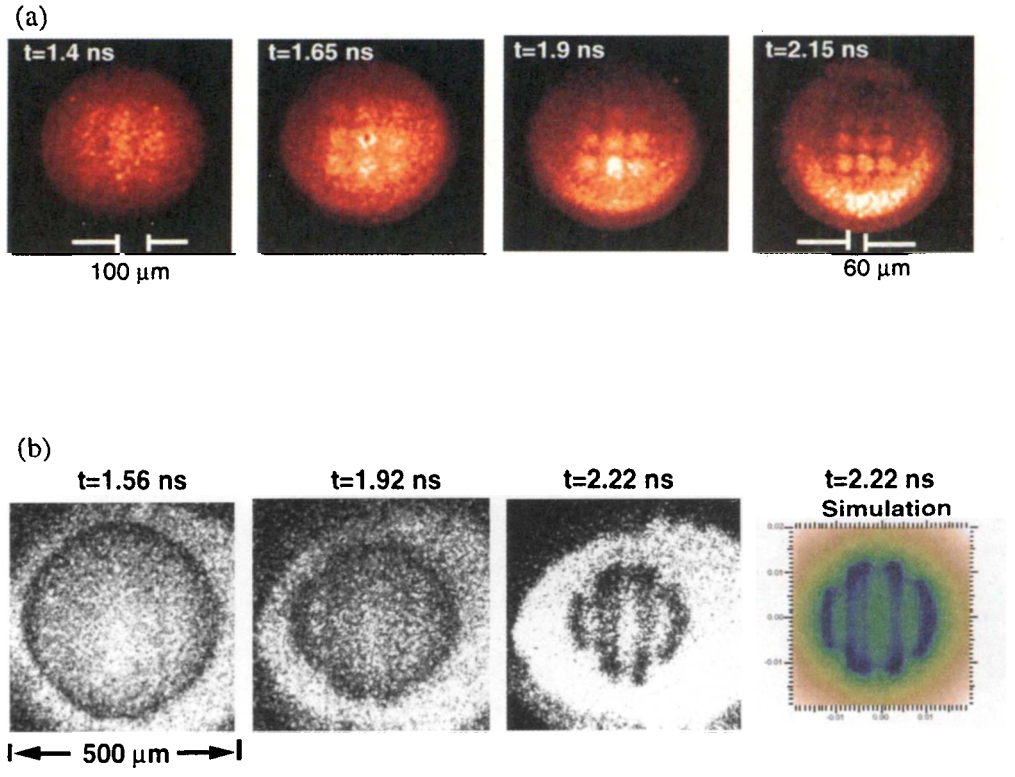

FIGURE 5. Initial results from Glendinning *et al.* (1997) and Cherfils *et al.* (1997a,b) of an experiment on the Nova laser very similar to that shown in figure 4a in spherically convergent geometry. A 3D $k_x = k_y$ ($\lambda_x = \lambda_y = 100$ μm) square perturbation, $\eta_0 = 2.5$ μm, was imposed on the outside of a 500-μm-diameter hemisphere of a CH(Ge) capsule and mounted on the wall of a hohlraum. This hemisphere is ablatively imploded with an X-ray drive, during which time the perturbation grows by the Rayleigh-Tayler instability. (a) Face-on, in-flight radiographs of the perturbation growing as it implodes. (b) Similar experiment by Kalantar *et al.* (1997b) on a full capsule implosion, where the capsule was mounted at the center of the hohlraum. The perturbations were three grooved rings scored into the capsule.

simulated perturbation peak-to-valley growth factor is about 10. An extensive set of convergent RT instability experiments in cylindrical geometry has recently been completed, showing instability evolution during convergence through stagnation and bounce (Hsing *et al.* 1997a,b).

The issue of macroscopic (say, as in nuclear testing) *versus* microscopic (such as Nova or NIF) experiments needs to be addressed. As an example, figure 6a shows data taken by Jacobs and Catton (1988) from a macroscopic (12 cm) water cell experiment, and figure 6b shows the results of Marinak *et al.* from the microscopic (500 μm) Nova experiment (Marinak *et al.* 1995; Remington *et al.* 1996b,c), both looking at the 3D RT evolution of a square $k_x = k_y$ surface perturbation. Figure 6b is the average of the central 16 perturbations shown in figure 4a displayed in a 3D perspective similar to the water cell data. The water experiment was done with a pressure of about 0.1 bar, accelerating a 2-L water cell at 5 g_0 with no compression or radiation, and was diagnosed by side-on optical shadowgraphy. The data shown in figure 6a were taken at $t = 50$ ms. The Nova experiment was done at a pressure of 30 Mbar, accelerating an initially 60-μm-thick CH(Br) foil at 7×10^{12} g_0 under high compression (5 times solid), with high levels of radiation flow, and diagnosed by face-on X-ray backlighting. The image shown in figure 6b was taken at $t = 4.3$ ns. The microscopic imaging capabilities on Nova are impressive (Kilkenny 1992), with as much detail observable in the Nova experiment as in the

https://doi.org/10.1017/S0263034600011186 Published online by Cambridge University Press

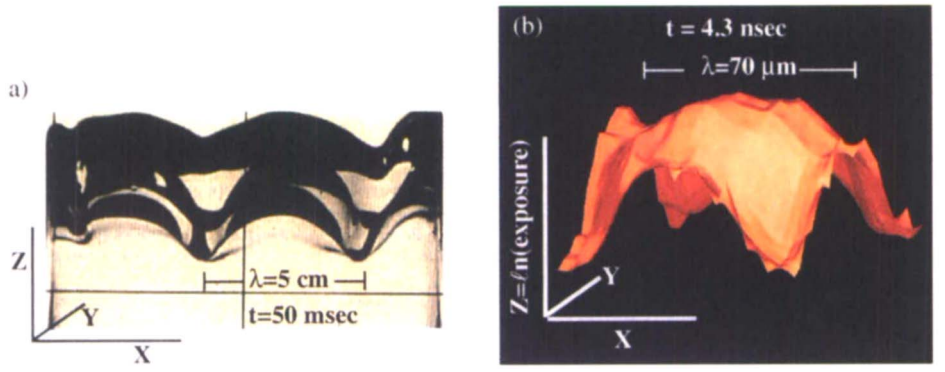

FIGURE 6. Comparison of 3D $k_x = k_y$ single-mode Rayleigh-Taylor data taken by (a) Jacobs and Catton (1988) on a 12-cm 5-g_0 macroscopic water-cell accelerator and (b) Marinak *et al.* (1995) on a 500-μm 10^{13}-g_0 accelerated foil at the Nova laser.

macroscopic water experiment. In comparing these two experiments, the spatial scales differ by 3 orders of magnitude, the time scales by 7 orders of magnitude, the pressures by over 8 orders of magnitude, and the accelerations differ by 12 orders of magnitude!

Figure 6 presents the opportunity to compare similar hydrodynamics in regimes of vastly different scale. In the nonlinear regime, the fluid flow can be characterized by a spatial scale of order, the perturbation wavelength λ, and velocity of order, the perturbation terminal bubble velocity $v_B \approx 0.3(g\lambda)^{1/2}$. Hence a hydrodynamic time scale can be approximated by $\tau = \lambda/v_B = (\lambda/g)^{1/2}$, dropping factors of 2. One gets the same result in the linear regime by writing the characteristic time as $\tau = \gamma^{-1} = (kg)^{-1/2} = (\lambda g)^{1/2}$, again dropping factors of 2. Hence, the scale transformation taking λ to $a_1\lambda$ and g to $a_2 g$ requires that τ goes to $(a_1/a_2)^{1/2}\tau$ for the hydrodynamic equations to be invariant (Hecht *et al.* 1994, 1995; Shvarts *et al.* 1995).

Based on the similar shapes of the perturbations shown in figure 6a,b, these two experiments appear to be accessing the same nonlinear hydrodynamics, so we can test this scale transformation. The scale factors relating spatial scale and acceleration are given by $a_1 = \lambda_{\text{micro}}/\lambda_{\text{macro}} = 1.4 \times 10^{-3}$ and $a_2 = g_{\text{micro}}/g_{\text{macro}} = 1.4 \times 10^{12}$, where the subscripts micro and macro refer to the laser and water cell experiments, respectively. The corresponding scaled time for the laser experiment is then given by $\tau = (a_1/a_2)^{1/2}(5 \times 10^{-2}\text{ s}) = 1.6 \times 10^{-9}$ s. This result compares well with the actual $\tau_{\text{RT}} = 4.3 - 2.5 = 1.8$ ns of the laser experiment in figure 6b, which represents the duration of foil acceleration after shock breakout, which occurs at 2.5 ns. Scale transformations of the hydrodynamics equations are straightforward, and one can learn much from simple experiments on incompressible fluids.

A quantitative understanding of hydrodynamic mixing relevant to ICF, nuclear applications, and astrophysics, however, requires experiments to be done at high compression with radiation flow. Rapid material compression leads to the launching of strong shocks, which generate material mixing through the RM instability (Dimonte *et al.* 1993, 1995, 1996a; Miller *et al.* 1995; Peyser *et al.* 1995; Velikovich & Dimonte 1996). Radiation flow leads to density gradients and to mass ablation, both of which can affect the degree of instability growth significantly. This effect is clearly illustrated in the recent Nova laser experiments of Budil *et al.* (1996) who compared RT growth at an ablation front with that at an RT-unstable embedded interface remote from the ablation front (figure 7). In this experiment, the target corresponded to a 35-μm doped plastic ($C_{50}H_{47}Br_3$) ablator, backed by a 15-μm Ti payload, with a 2D sinusoidal ripple at the plastic–metal interface. The experiments were conducted in an otherwise identical fashion to those described in figure 4, and the results are shown in figure 7 with

https://doi.org/10.1017/S0263034600011186 Published online by Cambridge University Press

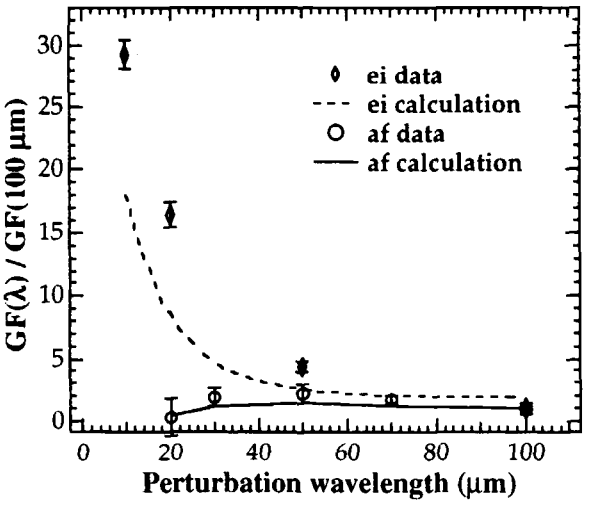

FIGURE 7. Experimental comparison of Budil *et al.* (1996) for Rayleigh-Taylor (RT)-induced perturbation growth at an ablation front (af) *versus* growth at an embedded interface (ei) remote from the ablation front. The ablation-front experiments (open circles) were identical to those illustrated in figure 4c for a range of 2D wavelengths. The embedded interface experiments were identical except that the 2D ripple was located at the interface between a 35-μm CH(Br) ablator and a 15-μm Ti payload. The curves are theoretical calculations. Due to the combined effects of density gradient and ablation velocity, the perturbation growth at the ablation front is strongly stabilized for $\lambda < 30$ μm.

the open-diamond plotting symbols. The largest perturbation GFs were observed for the shortest perturbation wavelengths, λ = 10–20 μm. For comparison, nearly identical experiments were also done with the perturbations at the ablation front, as shown by the open-circle plotting symbols. The growth of pertubations with $\lambda < 50$ μm was strongly inhibited. The combined effects of a density gradient and ablation velocity strongly stabilize growth of short wavelength perturbations at the ablation front, with perturbations of $\lambda \leq 20$ μm essentially not growing at all. Conversely, at the embedded interface, it is precisely the shortest wavelength perturbations that exhibit the largest growth; the maximum observed growth factor in the experiment by Budil *et al.* was at the shortest wavelength imaged, λ = 10 μm. Scaled experiments using classical incompressible fluids and not taking into account strong radiation effects can be misleading, as dramatically illustrated in figure 7.

The flexibility of lasers makes the variety of experiments possible almost limitless. One example is a series of experiments designed to probe compressible nonlinear mixing in hot, radiative plasmas relevant to supernovae evolution (Glanz 1997; Kane *et al.* 1997; Remington *et al.* 1997). Another example is in a diametrically opposite parameter regime, that is, cool and dense as opposed to hot and diffuse. We describe a new hydrodynamics initiative on the Nova laser to study hydrodynamic instabilities in the solid state (Remington *et al.* 1996a; Kalantar *et al.* 1997). By controlling the strength of the initial shocks launched into a sample, one can compress and accelerate a metal foil while maintaining it in the solid state. This opens up the possibility of investigating the growth (or lack thereof) of perturbations at an RT-unstable interface, where the interface remains in the solid state. The corresponding RT dispersion curve is expected to be sensitive to the yield strength and viscosity of the compressed solid (Barnes *et al.* 1974; Swegle & Robinson 1989a,b). The recent laser experiments by Kalantar *et al.* (1997a; Hauer *et al.* 1996; Wark *et al.* 1990, 1992, 1996; Woolsey & Wark 1997) have demonstrated that a solid can be compressed with a hohlraum X-ray drive and dynamically diagnosed in the solid state (see figure 3). Experiments are commencing on Nova to measure the RT dis-

https://doi.org/10.1017/S0263034600011186 Published online by Cambridge University Press

persion curve of a solid *versus* a liquid RT-unstable interface at pressures of 3–5 Mbar. The goal is, first to demonstrate material strength stabilization and, second, to relate the solid-state RT dispersion curve measurements back to the lattice viscosity and yield point of compressed solid-state metal.

4. Radiation physics

Almost by definition, "high-energy-density physics" denotes a regime in which the emission and absorption of radiation (usually X rays) from stripped ions and the transport of that radiation form an important part of the energy balance of the medium. This regime includes the study of the atomic spectroscopy of isolated ions (Griem 1974), the study of complex radiation opacities (Inglis & Teller 1939; Mayer 1947; Moore 1949; Karzas & Latter 1961a,b; Cox & Taber 1976; Henry 1983; Hora & Henry 1983; Magee *et al.* 1984; Bar-Shalom *et al.* 1989; Albritton & Liberman 1994; Wilson & Liberman 1994; Iglesias 1995), and investigations of radiation transport under various conditions. Applications range from understanding the behavior of an inertial confinement fusion hohlraum (radiation cavity) to the significant role of new metal opacity theory in models of pulsating stars such as the beat Cepheids (Rogers & Iglesias 1994). A practical benefit of radiation physics is the development of the X-ray laser as a new technique for plasma diagnostics and potentially for other fields such as medical physics (DaSilva *et al.* 1992b).

A wide range of experiments have been developed on the Nova laser to address aspects of these problems. Results from the radiation transport experiment of Perry *et al.* (1994) are shown in figure 8. In this experiment, the transport of the radiation heat front through a millimeter-scale Au tube filled with low-density (ρ = 26 mg/cm^3) SiO_2 silicon aerogel foam was measured. The experimental technique was absorption spectroscopy of a thin Al foil at the end of the Au tube. The backlighter, samarium, has a broad *L*-band of emission centered around the line structure of Al at 1.5–1.6 keV. As the Al foil heats up from the propagation of the radiation heat front, higher ionization states are observed with time in the streaked absorption spectrum, as shown in the image in figure 8a and in the processed profiles in figure 8b. With the higher energies and longer drives expected on future lasers, this type of radiation transport

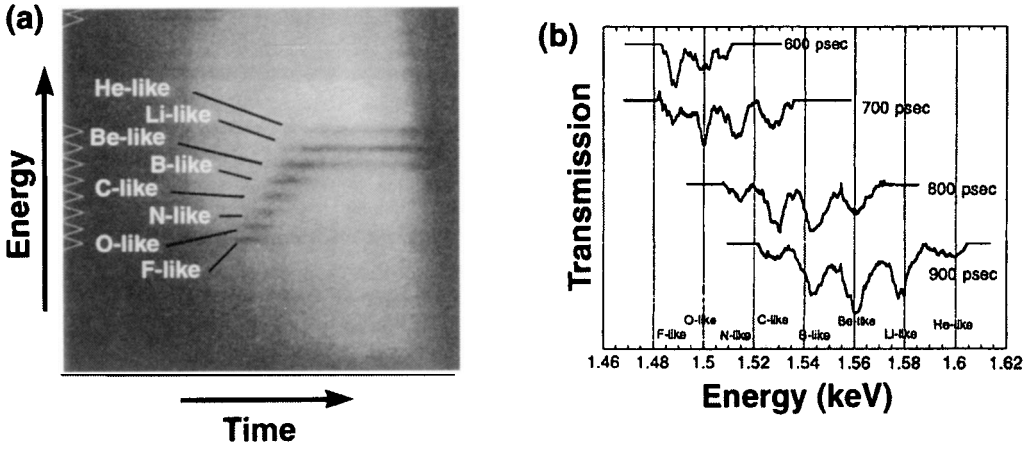

FIGURE 8. Results from Perry *et al.* (1994) of a Nova experiment to measure the transport of a radiation heat front. (a) The streaked absorption spectrum of an Al foil mounted at the end of a millimeter-scale Au tube filled with 26 mg/cm^3 silicon aerogel, back illuminated with a point backlighter of samarium. The radiative heat front moves farther down the tube with time, heating the Al sample to higher ionization states. (b) Lineouts through the streaked absorption spectrum for four time windows, again showing the higher ionization states of Al developing later in time.

https://doi.org/10.1017/S0263034600011186 Published online by Cambridge University Press

experiment could be extended to more complex and challenging geometries. For example, even on Nova, when using 30 kJ of total energy arranged temporally in a series of stacked 2-ns square pulses, one can generate a T_r = 80–100 eV radiation source lasting 15–20 ns. With the 2-MJ superlasers, long T_r sources should be straightforward and would undoubtedly be useful for the type radiation flow experiments described above.

Opacity experiments have been done with the Nova laser for a number of years (Perry *et al.* 1991; DaSilva *et al.* 1992a; Springer *et al.* 1992) and have evolved into a mature experimental tool. The technique relies on the ability to prepare a uniform X-ray–heated sample in local thermodynamic equilibrium (LTE), thereby allowing measurements of opacity through point projection absorption spectroscopy. Figure 9a shows the results for such a transmission spectrum (DaSilva *et al.* 1992; Perry *et al.* 1992; Rogers & Iglesias 1994) for Fe at a temperature of 20 eV and density of 0.008 g/cm^3. Figure 9b shows a similar result for aluminum (Perry *et al.* 1991) at 58 eV and 0.02 g/cm^3. Both experimental results are compared with calculations using the modern detailed accounting code OPAL (Rogers & Iglesias 1994). The interest in the Fe opacity measurement was due to its relevance to the problem of the pulsation period of beat Cepheid stars (Rogers & Iglesias 1994). Furthermore, the EOS foundations of OPAL are relevant to the problem of helioseismology of our sun (Christensen-Dalsgaard *et al.* 1996). The Al opacity was measured in an effort to develop a standard electron temperature (T_e) thermometer for Nova plasmas, as discussed below. The temperatures for these two opacity experiments (figure 9) were low. Opacities also can be probed at high temperature, where the interest turns to high-Z opacities. To generate the required high temperatures, high laser power needs to be focused into reduced scale hohlraums. By reducing the spatial scale of the hohlraums to a fraction of their typical size, temperatures of up to 400 eV or more seem possible on Nova. On NIF, the maximum temperature achievable should be significantly higher, making critical high-Z opacity measurements possible.

Based on the success of experiments and OPAL calculations of the opacities of Al (see figure 9b), this technique has evolved to the point where it is viewed as a standard electron temperature diagnostic. An application of this new T_e diagnostic is illustrated with a colliding Al plasma experiment (Perry *et al.* 1997) in figure 10. In this experiment, two thin Al foils initially separated by 180 μm are exploded on Nova with a pulsed, hard X-ray drive. The density of the evolving Al plasmas and their collision at the midpoint between them is measured by standard X-ray radiography (figure 10a). On a separate experiment using point projection absorption spectroscopy, the transmission spectrum is measured at 2 ns. Using the densities at 2 ns inferred

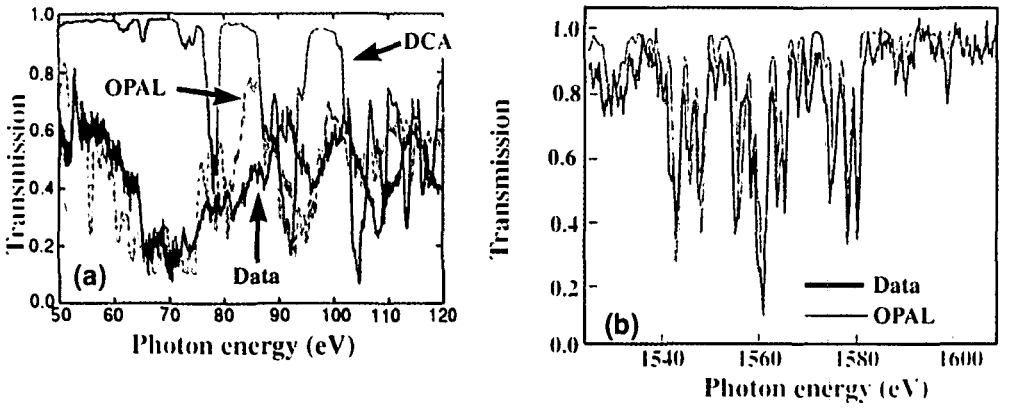

FIGURE 9. Nova experimental data of (a) DaSilva *et al.* (1992) and (b) Perry *et al.* (1991) for the LTE opacity of (a) iron and (b) Al *versus* the OPAL and DCA opacity model calculations. OPAL agrees better with the data than does DCA.

https://doi.org/10.1017/S0263034600011186 Published online by Cambridge University Press

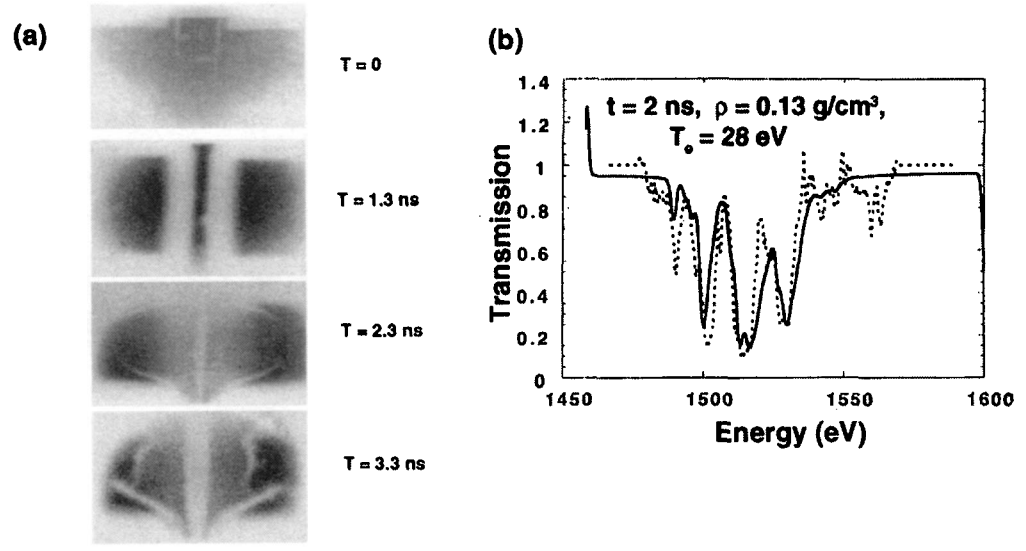

FIGURE 10. (a) Time sequence of radiographs of colliding Al plasmas from a Nova laser experiment of Perry *et al.* (1997). (b) Temperature measurement of the colliding Al plasma at 2 ns, based on point-projection spectroscopy measurements compared with OPAL simulations.

from figure 10a and OPAL calculations of the transmission spectrum expected as a function of T_e, the temperature of the colliding plasma is deduced to be 28 eV (figure 10b). This represents an excellent example of turning what was once considered a forefront research area at Nova into a practical T_e diagnostic.

The discovery and development of X-ray lasers (Elton 1990; Mathews 1994) is another excellent example of forefront non-LTE laser plasma research leading to the development of a useful diagnostic. Figure 11a shows how the X-ray laser's extraordinary effective brightness (10^{17} W/cm^2-Å-ster, which is the equivalent of a 6-GeV black body) is being used to image the column densities of hot dense plasmas down to the micron scale with 50-ps time resolution (Cauble *et al.* 1995). In this experiment, a planar target consisting of 10 μm of CH, backed by 3 μm of Al, was accelerated by direct illumination on the CH side with a 1-ns Nova pulse at $\lambda_{\text{Laser}} = 528$ nm and intensity of $I \approx 1 \times 10^{14}$ W/cm^2. The laser was incident from below, generating pressures of ~20 Mbar, which accelerated the foil at $\sim 10^{13}\ g_0$, where g_0 is the acceleration due to gravity. The foil was originally located at zero on the vertical scale. The foil was viewed across the back edge at 1.1 ns with side-on radiography, using an X-ray laser as the backlighter. Fine striations down to 5-μm features in the Al plasma blowoff, represented by the dark regions in the image, are easily resolved with this X-ray imaging diagnostic. The X-ray laser is also being explored as a potential tool for use in the medical field for precise imaging of microscopic biological specimens (DaSilva *et al.* 1992b).

X-ray laser interferometry has been developed by DaSilva *et al.* into an electron density (n_e) diagnostic (DaSilva *et al.* 1995), an example of which is shown in figure 11b (DaSilva *et al.* 1996). With this interferometer, a 2-mm-long foil consists of 80 nm of Se coated on 100 nm of lexan. One Nova beam in a 120-μm-line-focus configuration and an intensity of 7×10^{13} W/cm^2 irradiates the foil. The view in the image shown in figure 11b is end-on, with the laser incident from below. The unirradiated part of the foil can be seen as the horizontal shadow near 0 μm on the vertical scale. The short duration of the X-ray laser backlighter pulse (200 ps) makes the interferogram a "snapshot," which was timed to be at 500 ps after the start of the heating pulse. Spatial resolution is about 2 μm. Two pockets of self-emission can be seen just

https://doi.org/10.1017/S0263034600011186 Published online by Cambridge University Press

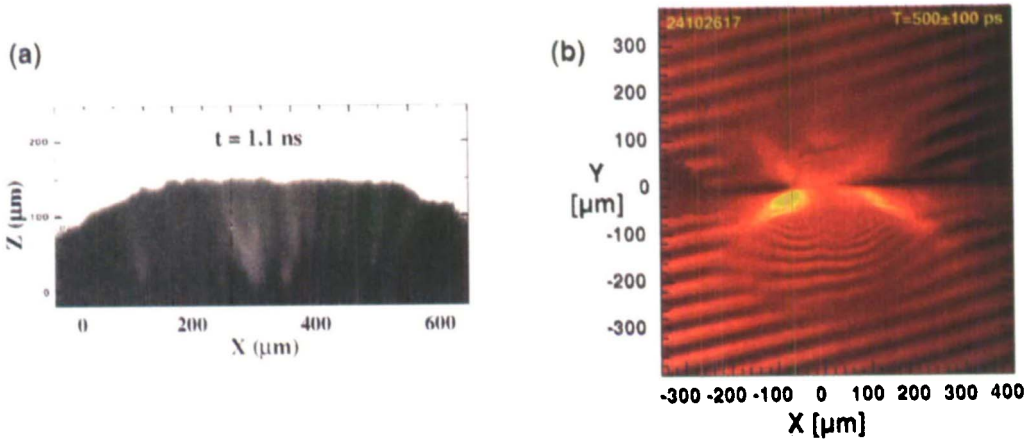

FIGURE 11. (a) Side-on X-ray laser radiograph from an experiment of Cauble *et al.* (1995) using the Nova laser. The radiograph was taken at 30× magnification at time 1.1 ns of a foil accelerated by direct illumination with a 1-ns Nova pulse at wavelength $\lambda_{Laser} = 528$ nm and intensity $I = 10^{14}$ W/cm^2. The foil consisted of a 10-μm CH ablator backed by a 3-μm Al payload. The laser was incident on the CH ablator from below, generating pressures of ~20 Mbar, which accelerated the foil at 10^{13} g_0, where g_0 is the acceleration due to gravity. The foil was originally located at zero on the vertical scale. (b) Sample interferogram taken by DaSilva *et al.* (1996) using the Nova laser to create an the X-ray laser interferometer. The view is end-on to a line focus illuminated (from below) at $\lambda_{Laser} = 528$ nm onto a Se foil.

off the surface. The twin-lobed blowoff structure, as indicated by the two regions of different fringe curvature (and thus different electron density profiles) on either side of the center line, likely results from structure in the drive laser. Peak electron densities in the central region are measured to be about 4×10^{20} cm^{-3}, much higher than can be achieved in optical interferometry. This diagnostic has since been used to characterize colliding Au plasmas (Wan *et al.* 1997). This experiment was qualitatively similar to that shown in figure 10, except that the colliding plasmas were Au and n_e was diagnosed with the X-ray interferometer. The result was an experimental demonstration that even high-Z plasmas initially interprenetrate when they collide, an effect that cannot be modeled with a Lagrangian fluids code. Simulations with a particle-in-cell (PIC) code, however, were in much better agreement with the data. Hence, this is an excellent example of using well-diagnosed laser experiments to establish regimes of validity of various computer models.

5. Summary

Nuclear detonation experiments offer the unique possibility of bringing very large volumes of material into high-energy-density conditions. However, such experiments are expensive, difficult to diagnose with high precision, and currently prohibited under a comprehensive test-ban treaty. In contrast, the megajoule-class superlasers such as the NIF will be able to conduct multiple-shot experimental campaigns over time frames of days or weeks. Therefore, the laser experiments offer the possibility of extensive parameter variation, control, and diagnostic development. Examples of this ability to control the experiments are the ubiquitous use of timed X-ray backlighters (1) to allow EOS measurements at 10s to 100s of megabar pressures, (2) to "stop-action photograph" hydrodynamic instabilities in evolution, (3) to measure time-resolved LTE opacities of samples prepared at various densities and temperatures, and (4) to record the progression of a radiation heat front. The routine quantitative examination of matter with these enormously capable and flexible facilities will invigorate and firmly establish the field of high-energy-density physics. With the cessation of nuclear testing, some re-

https://doi.org/10.1017/S0263034600011186 Published online by Cambridge University Press

gimes of high-energy-density physics will be lost, but a considerable subset will be accessible with much greater control and reproducibility with the superlasers.

Acknowledgments

This work was performed under the auspices of the U.S. Department of Energy by the Lawrence Livermore National Laboratory under contract No. W-7405-ENG-48. We have drawn on the superb work of scores of scientists in compiling the results discussed in this paper. We regret any oversights of specific pieces of work, and emphasize that any such omissions were unintentional.

REFERENCES

AL'TSCHULER, L.V. 1965 *Sov. Phys. Uspekhi* **8**, 52.

ALBRITTON, J.R. & LIBERMAN, D.A. 1994 *JQSRT* **51**, 9.

ANDRE, M. 1995 *First Annual International Conf. on Solid State Lasers for Application to ICF* (Monterey, CA).

ANDRIYASH, A.V. & SIMONENKO, V.A. 1984 *Topics Atomic Sci. Technol.* **2**, 52.

AVRORIN, E. *et al.* 1987 *Sov. Phys. JETP* **66**, 348.

AVRORIN, E.N. *et al.* 1993 *Phys. Uspekhi* **36**, 337.

BAR-SHALOM, A. *et al.* 1989 *Phys. Rev. A* **40**, 3183.

BARNES, J.F. *et al.* 1974 *J. Appl. Phys.* **45**, 727.

BENJAMIN, R.F. & FRITZ, J.N. 1987 *Phys. Fluids* **30**, 331.

BETHE, H.A. 1995 *Science* **269**, 1455.

BODNER, S.E. 1974 *Phys. Rev. Lett.* **33**, 761.

BONAZZA, R. & STURTEVANT, B. 1996 *Phys. Fluids* **8**, 2496.

BROUILLETTE, M. & STURTEVANT, B. 1994 *J. Fluid Mech.* **263**, 271.

BRUECKNER, K.A. *et al.* 1974 *Phys. Fluids* **17**, 1554.

BUDIL, K.S. *et al.* 1996 *Phys. Rev. Lett.* **76**, 4536.

BULANOV, S.V. *et al.* 1996 *Physica Scripta* **T63**, 280.

CAMPBELL, E.M. 1991 *Lasers Part. Beams* **9**, 209.

CAMPBELL, E.M. *et al.* 1995 In *Proc. of the 1995 APS Topical Conf. on Shock Compression of Condensed Matter* (Seattle, WA).

CAUBLE, R.C. *et al.* 1993 *Phys. Rev. Lett.* **70**, 2102.

CAUBLE, R.C. *et al.* 1995 *Phys. Rev. Lett.* **74**, 3816.

CAUBLE, R.C. *et al.* 1997 *Phys. Plasmas* **4**, 1857.

CERNIELLO, C. 1996 (Sept.) *Arms Control Today* **26**, 21.

CHERFILS, C. *et al.* 1997a In *Proc. of the LIRPP Conf.* (in press).

CHERFILS, C. *et al.* 1997b *Proc of the 6th Int. Workshop on the Physics of Compressible Turbulent Mixing* (Marseille, France) (in press).

CHEVALIER, R. & BLONDIN, J. 1995 *Ap. J.* **444**, 312.

CHOCS No. 13 1995 *Rev. Sci. Tech. Dir. Appl. Milit.*

CHRISTENSEN-DALSGAARD, J. *et al.* 1996 *Science* **272**, 1286.

COX, A.N. & TABER, J.E. 1976 *Ap. J. Suppl.* **31**, 271.

DAHLBURG, J.P. *et al.* 1993 *Phys. Fluids B* **5**, 571.

DA SILVA, L.B. *et al.* 1992a *Phys. Rev. Lett.* **69**, 438.

DA SILVA, L.B. *et al.* 1992b *Science* **258**, 269.

DA SILVA, L.B. *et al.* 1995 *Phys. Rev. Lett.* **74**, 3991.

DA SILVA, L.B. *et al.* 1996 *IEEE Trans. Plasma Sci.* **24**, 31.

DA SILVA, L.B. *et al.* 1997 *Phys. Rev. Lett.* **78**, 483.

DIMONTE, G. & REMINGTON, B.A. 1993 *Phys. Rev. Lett.* **70**, 1806.

https://doi.org/10.1017/S0263034600011186 Published online by Cambridge University Press

DIMONTE, G. *et al.* 1995 *Phys. Rev. Lett.* **74**, 4855.

DIMONTE, G. *et al.* 1996a *Phys. Plasmas* **3**, 614.

DIMONTE, G. *et al.* 1996b *Rev. Sci. Instr.* **67**, 302.

EDER, D.C. & MATHEWS, D.L. 1994 *X-Ray Lasers 1994: 4th International Colloquium, AIP Conf. Proc. 332.*

ELIEZER, S. & RICCHI, R.A., eds. 1991 *High Pressure Equations of State: Theory and Applications* (North Holland, Amsterdam).

ELIEZAR, S. *et al.* 1986 *Equations of State* (Cambridge University Press).

ELTON, R. 1990 *X-Ray Lasers* (Academic Press, New York).

EVANS. A.M. *et al.* 1996a *Laser Part. Beams* **14**, 113.

EVANS, A.M. *et al.* 1996b In *Proc. of the Laser Interactions with Matter* (Oxford University Press), p. 235.

FARAL, B. *et al.* 1990 *Phys. Fluids B* **2**, 371.

FORTOV, V.E. & KOSTIN, V.V. 1991 *J. Appl. Phys.* **70**, 4524.

FU, S. *et al.* 1995 *Phys. Plasmas* **2**, 3461.

GLANZ, J. 1997 *Science* **276**, 351.

GLENDINNING, S.G. *et al.* 1997 *Proc. of the 6th International Workshop on the Physics of Compressible Turbulent Mixing* (Marseille, France) (in press).

GOODWIN, I. 1996 (Dec.) *Physics Today* **49**, 37.

GRIEM, H. 1974 *Spectral Line Broadening by Plasmas* (Academic Press, New York).

HAMMEL, B.A. *et al.* 1993 *Phys. Fluids* **5**, 2259.

HAMMEL, B.A. *et al.* 1994 *Phys. Plasmas* **1**, 1662.

HARTEMANN, F.V. *et al.* 1995 *Phys. Rev. E* **51**, 4833.

HAUER, A. *et al.* 1996 *Bull. Am. Phys. Soc.* **41**, 1600.

HECHT, J. *et al.* 1995 *Laser Part. Beams* **13**, 423.

HENDERSON, D.B. *et al.* 1975 *Phys. Rev. Lett.* **33**, 205.

HENRY, B.I. 1983 *Laser Part. Beams* **1**, 11.

HOLIAN, K.S. 1984 *T-4 Handbook of Material Properties Data Bases*, Vol. 1C EOS LA-10160-MS.

HOLMES, N.C. 1991 *High-Pressure Science and Technology*, S.C. Schmidt *et al.*, eds. (AIP, New York), p. 153.

HOLMES, N.C. *et al.* 1984 *Appl. Phys. Lett.* **45**, 626.

HOLMES, N.C. *et al.* 1995 *Phys. Rev. B* **52**, 15835.

HORA, H. 1991 *Plasmas at High Temperature and Density* (Springer-Verlag, Heidelberg).

HORA, H. & HENRY, B.I. 1983 *Opt. Commun.* **44**, 218.

HSING, W. *et al.* 1997a *Phys. Rev. Lett.* **78**, 3876.

HSING, W. *et al.* 1997b *Phys. Plasmas* **4**, 1832.

HUBBARD, W.B. 1997 *Phys. Plasmas* **4**, 2011.

HUBBARD, W.B. *et al.* 1995 In *Elementary Processes in Dense Plasmas: Proc. of the Oji International Seminar*, S. Ichimaru & S. Ogata, eds. (Addison-Wesley, Menlo Park, CA), p. 227.

HUBBARD, W.H. & DEWITT, H.E. 1985 *Ap. J.* **290**, 388.

IGLESIAS, C.A. 1995 *JQSRT* **54**, 185.

INGLIS, D.R. & TELLER, E. 1939 *Ap. J.* **90**, 439.

JACOBS, J.W. & CATTON, I. 1988 *J. Fluid Mech.* **187**, 353.

JACOBS, J.W. & SHEELEY, J.M. 1996 *Phys. Fluids* **8**, 405.

KALANTAR, D.H. *et al.* 1997 *Proc. of the 6th International Workshop on the Physics of Compressible Turbulent Mixing* (Marseille, France) (in press).

KALANTAR, D.H. *et al.* 1997a *Annual Meeting of the American Crystallographic Assoc.* (St. Louis, MO).

KALANTAR, D.H. *et al.* 1997b *Rev. Sci. Instr.* **68**, 814.

KANE, J. *et al.* 1997 *Ap. J.* **478**, L75.

KARZAS, W.J. & LATTER, R. 1961a *Ap. J.* **134**, 665.

KARZAS, W.J. & LATTER, R. 1961b *Ap. J. Suppl.* **6**, 167.

KEENY, S.M. JR. & CERNIELLO, C. 1996 (Aug) *Arms Control Today* **26**, 15.

KILKENNY, J.D. 1992 *Rev. Sci. Instr.* **63**, 4688.

https://doi.org/10.1017/S0263034600011186 Published online by Cambridge University Press

KITTEL, C. 1976 *Principles of Solid State Physics*, 5th ed. (John Wiley, New York), p. 64.

KLEIN, R.I. *et al.* 1994 *Ap. J.* **420**, 213.

KOENIG, M. 1995 *Phys. Rev. Lett.* **74**, 2260.

KOPYSHEV, V.P. 1977 *Chisl. Metody Mekh Splosh. Sred* **8**, 54.

KUCHERENKO, Y.A. *et al.* 1991 In *Proc. of the 3rd International Workshop on the Physics of Compressible Turbulent Mixing* (Royaumont, France), p. 427.

KUCHERENKO, Y.A. *et al.* 1993 In *Proc. of the 4th International Workshop on the Physics of Compressible Turbulent Mixing* (Cambridge, UK), pp. 57, 70, 129.

LAWLER, A. 1997 *Science* **275**, 1254.

LEE, R.W. *et al.* 1995 UCRL-LR-119170; http://www.llnl.gov/tid/lof/documents/citation-action-page/228189.html

LIBERMAN, D.A. 1982 *JQSRT* **27**, 335.

LINDL, J. 1995 *Phys. Plasmas* **2**, 3933.

LINDL, J.D. & MEAD, W.C. 1975 *Phys. Rev. Lett.* **34**, 1273.

LÖWER, T. & SIGEL, R. 1993 *Contrib. Plasma Phys.* **33**, 355.

LÖWER, T. *et al.* 1994 *Phys. Rev. Lett.* **72**, 3186.

LUO, D. & MCCRAY, R. 1991 *Ap. J.* **379**, 659.

LUO, D. & MCCRAY, R. 1994 *Ap. J.* **430**, 264.

MAGEE, N.H., JR., *et al.* 1984 *Ap. J.* **283**, 264.

MARINAK, M. *et al.* 1995 *Phys. Rev. Lett.* **75**, 3677.

MARLEY, M.S. & HUBBARD, W.B. 1988 *Icarus* **73**, 536.

MASON, R.J. 1996 In *26th Anomalous Absorption Conf.* (Fairbanks, AK).

MAYER, H. 1947 Los Alamos Report LA647 (AECD-1870).

MAYER, M.G. 1941 *Phys. Rev.* **60**, 184.

MCKAY, A. 1984 *The Making of the Atomic Age* (Oxford University Press, New York).

MEYER-TER-VEHN, J. & OPARIN, A. 1995 In *Elementary Processes in Dense Plasmas: Proc. of the Oji International Seminar*, S. Ichimaru & S. Ogata, eds. (Addison-Wesley, Menlo Park, CA), p. 283.

MEYERS, M.A. 1994 *Dynamic Behavior of Materials* (John Wiley, New York).

MILLER, P. *et al.* 1995 In *Proc. of the 20th International Symp. of Shock Waves* (Pasadena, CA).

MITCHELL, A.C. 1991 *J. Appl. Phys.* **69**, 2981.

MOORE, C.E. 1949 *NBS Circ.* **467**, 1.

MÜLLER, E. *et al.* 1991 *Astron. Astrophys.* **251**, 505.

NELLIS, W.J. 1984 *Phys. Rev. Lett.* **53**, 1661.

NELLIS, W.J. 1995 *Science* **269**, 1249.

NELLIS, W.J. *et al.* 1991 *J. Chem. Phys.* **94**, 2244.

NIKIFOROV, A.F. *et al.* 1978 *Vopr. At. Nauki Tekh.* **3**, 62.

NIKIFOROV, A.F. *et al.* 1979 *Vopr. At. Nauki Tekh.* **4**, 16.

NIKIFOROV, A.F. *et al.* 1989 *Mathematical Simulation: Physical–Chemical Properties of Matter* (Nauka, Moscow), p. 162.

NISHIHARA, K. & SAKAGAMA, H. 1990 *Phys. Rev. Lett.* **65**, 432.

NUCKOLLS, J. *et al.* 1972 *Nature* **239**, 139.

PAISNER, J.A. *et al.* 1994 *Fusion Technol.* **26**, 755.

PERRY, M.D. & MOUROU, G. 1994 *Science* **264**, 917.

PERRY, T.S. *et al.* 1991 *Phys. Rev. Lett.* **67**, 3784.

PERRY, T.S. *et al.* 1994 *JQSRT* **51**, 273.

PERRY, T.S. *et al.* 1997 *Phys. Rev. E* (submitted).

PEYSER, T.A. 1995 *Phys. Rev. Lett.* **75**, 2332.

PUKHOV, A. & MEYER-TER-VEHN, J. 1996 *Phys. Rev. Lett.* **76**, 3975.

RADOUSKY, H.B. *et al.* 1986 *Phys. Rev. Lett.* **57**, 2419.

RAGAN, C.E. III *et al.* 1997 *J. Appl. Phys.* **48**, 2860.

READ, K.I. 1984 *Physica D* **12**, 45.

https://doi.org/10.1017/S0263034600011186 Published online by Cambridge University Press

REMINGTON, B.A. *et al.* 1997 *Phys. Plasmas* **4**, 1994.

REMINGTON, B.A. *et al.* 1996a *Bull. Am. Phys. Soc.* **41**, 1354.

REMINGTON, B.A. *et al.* 1996b *Proc. of the 5th International Workshop on Compressible Turbulent Mixing*, R. Young *et al.*, eds. (World Scientific, NJ), p. 265.

REMINGTON, B.A. *et al.* 1996c In *Proc of the LIRPP Conf.*, S. Nakai & G.H. Miley, eds. (AIP Press, NY), p. 115.

ROGERS, F.J. 1981 *Phys. Rev. A* **24**, 1531.

ROGERS, F.J. & IGLESIAS, C.A. 1994 *Science* **263**, 50.

ROSEN, M. 1996 *Phys. Plasmas* **3**, 1803.

ROSS, M. 1987 *J. Chem. Phys.* **86**, 7110.

SAUMON, D. & CHABRIER, G. 1992 *Phys. Rev. A* **46**, 2084.

SCHNEIDER, M. *et al.* 1997 In *Proc. of the 6th Int. Workshop on the Phys. of Compressible Turbulent Mixing* (Marseille, France) (in press).

SHVARTS, D. *et al.* 1995 *Phys. Plasmas* **2**, 2465.

SIMONENKO, V.A. *et al.* 1985 *Sov. Phys. JETP* **61**, 869.

SIN'KO, G.V. 1979 *Teplofix. Vys. Temp.* **2**, 1041.

SPRINGER, P.T. *et al.* 1992 *Phys. Rev. Lett.* **69**, 3735.

STEVENSON, D.J. 1975 *Phys. Rev. B* **12**, 3999.

STEVENSON, D.J. 1976 *Phys. Lett.* **58A**, 282.

SUZUKI, T. *et al.* 1993 *Astron. Astrophys.* **274**, 883.

SWEGLE, J.W. & ROBINSON, A.C. 1989a *J. Appl. Phys.* **66**, 2838.

SWEGLE, J.W. & ROBINSON, A.C. 1989b *J. Appl. Phys.* **66**, 2859.

TABAK, M. *et al.* 1993 *Phys. Plasmas* **1**, 2010.

TELLER, E. 1987 *Encyclopedia of Physical Science and Technology*, Vol. 5 (Academic Press, New York), p. 723.

TOWN, R.P.J. & BELL, A.R. 1991 *Phys. Rev. Lett.* **67**, 1863.

TRUNIN, R.F. 1994 *Phys. Uspekhi* **37**, 1123.

TRYGGVASON, G. & UNVERDI, S.O. 1990 *Phys. Fluids A* **2**, 656.

UMSTADTER, D. *et al.* 1995 *JQSRT* **54**, 401.

UMSTADTER, D. *et al.* 1996 *Science* **273**, 472.

VELIKOVICH, A.L. & DIMONTE, G. 1996 *Phys. Rev. Lett.* **76**, 3112.

VETTER, M. & STURTEVANT, B. 1995 *Shock Waves* **4**, 247.

WAN, A.S. *et al.* 1997 *Phys. Rev. E* **55**, 6293.

WARK, J.S. *et al.* 1987 *Phys. Rev. B* **35**, 9391.

WARK, J.S. *et al.* 1989 *Phys. Rev. B* **40**, 5705.

WARK, J.S. *et al.* 1990 *J. Appl. Phys.* **68**, 4531.

WARK, J.S. *et al.* 1992 *Appl. Phys. Lett.* **61**, 651.

WARK, J.S. *et al.* 1996 *Bull. Am. Phys. Soc.* **41**, 1600.

WEIR, S.T. *et al.* 1996 *Phys. Rev. Lett.* **76**, 1860.

WEISMAN, J. 1995 *Science* **270**, 21.

WHITLOCK, R.R. & WARK, J.S. 1995 *Phys. Rev. B* **52**, 8.

WILKS, S.C. *et al.* 1992 *Phys. Rev. Lett.* **69**, 1383.

WILKS, S.C. *et al.* 1993 *Phys. Fluids* **5**, 2603.

WILSON, B.G. & LIBERMAN, D.A. 1994 *JQSRT* **54**, 427.

WOOLSEY, N.C. & WARK, J.S. 1997 *J. Appl. Phys.* **81**, 3023.

YOUNG, D.A. *et al.* 1985 *Phys. Lett.* **108A**, 157.

YOUNGS, D.L. 1984 *Physica D* **12**, 32.

ZARETSKII, E.B. *et al.* 1991 *Sov. Phys. Dokl.* **36**, 76.

ZEL'DOVICH, Y.B. & RAIZER, Y.P. 1967 *Physics of Shock Waves and High-Temperature Hydrodynamic Phenomena* (Academic Press, New York).

https://doi.org/10.1017/S0263034600011186 Published online by Cambridge University Press